Journal of Sound and Vibration 520 (2022) 116638

Contents lists available at ScienceDirect

Journal of Sound and Vibration

journal homepage: www.elsevier.com/locate/jsvi

Beamforming for measurements under disturbed propagation conditions using numerically calculated Green's functions

Marius Lehmann [a,*], Daniel Ernst [b], Marc Schneider [a], Carsten Spehr [b], Markus Lummer [c]

[a] ebm-papst Mulfingen GmbH & Co. KG, Bachmühle 2, D-74673 Mulfingen, Germany
[b] German Aerospace Center (DLR), Bunsenstr. 10, D-37073 Göttingen, Germany
[c] German Aerospace Center (DLR), Lilienthalplatz 7, D-38108 Braunschweig, Germany

ARTICLE INFO

MSC:
00-01
99-00

Keywords:
Beamforming
Disturbed sound propagation
Boundary element method
Steering vector formulation
Tailored Green's functions

ABSTRACT

Beamforming methods for sound source localization are usually based on free-field Green's functions to model the sound propagation between source and microphones. This assumption is known to be incorrect for many industrial applications and the beamforming results can suffer from this inconsistency regarding both, main lobe width and dynamic range. The aim of this paper is to investigate whether the use of numerically calculated Green's functions, which include the diffraction and reflection of the sound path between source and microphones, can improve the results of beamforming measurements.

The current test cases of numerical and experimental investigations consist of a source placed in a short rectangular duct. The measurements are performed outside the duct in a semi-anechoic chamber. A typical example for this kind of installation is a fan with a heat exchanger.

The Green's functions for this test case are calculated numerically using the boundary element method. These tailored Green's functions are used to calculate the corresponding beamforming steering vectors.

Beamforming measurements are performed in this paper using a loudspeaker mounted in a disc as a reference source in the heat exchanger duct. The measurements are performed both with stationary and rotating disc. The stationary measurements are evaluated in the frequency domain. For the evaluation of the rotating measurements, a new beamforming method in the time domain is presented. This method also uses the stationary Green's functions, which were calculated numerically in the frequency domain. It is also shown how the weighting of these tailored Green's functions can be done for time domain beamforming.

By means of different validation criteria it can be shown that the results with the numerical calculated Green's functions are improved compared to free field beamforming. This is true both in the stationary and rotating case.

1. Introduction

Reliable knowledge about aeroacoustic sound sources on fans plays a decisive role in the development of quiet fans. Therefore, the experimental localization of sound sources on fan blades during rotation is an important task on the path to understanding

* Corresponding author.
E-mail address: Marius.Lehmann@de.ebmpapst.com (M. Lehmann).
URL: https://www.ebmpapst.com (M. Lehmann).

https://doi.org/10.1016/j.jsv.2021.116638
Received 27 October 2020; Received in revised form 22 October 2021; Accepted 16 November 2021
Available online 30 November 2021

Nomenclature

A	Source power
b	Main lobe width
c	Speed of sound
d	Diameter of ring array
E	Expectation operator
f	Frequency
$\hat{g}$	Green's function
K	Number of samples during time period
k	Sample index
L	Level
M	Number of microphones
m	Microphone index
Ma	Mach number
N_{sw}	Number of samples in impulse response
$\mathbf{p}$	Pressure vector
p	Pressure signal
$\hat{p}$	Complex pressure amplitude
r	Distance focus point/microphone
t	Time
w	Impulse response in time domain
$\hat{w}$	Steering vector in frequency domain
$\mathbf{y}$	Focus point
x, y, z	Cartesian coordinates
$\mathcal{F}^{-1}$	Inverse Fourier transform
$\bar{\sigma}(t, \mathbf{y})$	Estimated source signal
$\hat{\sigma}(f, \mathbf{y})$	Estimated source auto power
$(\cdot)^*$	Complex conjugate (transpose)
$(\cdot)_k$	For the kth sample
$(\cdot)_m$	For the mth microphone
$(\cdot)_n$	For the nth microphone
$(\cdot)_{\max}$	Maximum
$(\cdot)_S$	Sampling
$(\cdot)_s$	Source
$(\cdot)_{\mathrm{SL}}$	Side lobe
BEM	Boundary Element Method
CAA	Computational Aeroacoustics
CAD	Computer Aided Design
CSM, ($\mathbf{C}$)	Cross Spectral Matrix
FEM	Finite Element Method
FF	Free-field
FIR	Finite Impulse Response (filter)
FM	Fast Multipole
FMCAS	Fast Multipole Code for Acoustic Shielding
iFFT	inverse Fast Fourier Transform
ISM	Image Source Method
MSR	Main lobe to side lobe ratio
ppw	Points per wavelength
SPR	Source to pattern ratio

and reducing these rotating sources. For this purpose rotating beamforming methods based on microphone array measurements are applied. Barsikow et al. [1] were one of the first to use microphone arrays for noise research. A general overview of beamforming methods used nowadays is given by Meriono-Martinez et al. [2].

The main post-processing techniques to take into account the rotation of sources measured by a stationary array can be divided into two groups with regard to the implementation of rotation:

In the first group, the sound propagation from the rotating focus grid to the stationary microphones is modelled. The most important representative of this approach is the ROSI algorithm [3,4]. It is derived from the pressure field of a moving monopole in uniform flow. This approach is used to calculate the time dependent Green's functions (under free-field conditions) from a fan-fixed focus grid to the array microphones. Any microphone array layout can be taken into account.

In the second group, the stationary microphones in the array are virtually set into rotation. Therefore, the transfer functions between the sources on the rotating blades and the virtual with the same speed rotating microphones become time-independent. This makes it possible to perform the beamforming process in the frequency domain. The virtual rotation itself can be performed in both, time domain and frequency domain. The virtual rotation in the time domain was first presented by Dougherty et al. [5] and enhanced by Herold & Sarradj [6]. An example of a method that works completely in the frequency domain was presented by Lowis and Joseph [7,8] who investigated rotating sources in ducts. Pannert & Maier [9] and Ocker & Pannert [10] have adapted the method to free-space conditions. Most of the mentioned methods are limited to circular arrays. However, Jekosch [11] has extended the application of virtual rotation in the time domain to arbitrary array geometries.

The beamforming methods based on virtual rotating microphones can be used only for test cases where the sound propagation to the microphones takes place under free-field conditions or where both, fan and microphone array, are installed under rotationally symmetric conditions. However, a typical application for axial fans is the installation in a heat exchanger (Fig. 1). In most cases, the air is sucked through the heat exchanger by the fan. This creates a turbulent inflow that interacts with the fan blades and generates low frequency sound. In order to localize sound sources at low frequencies with sufficient narrow main lobe width, large microphone arrays have to be used. The sound propagation from the fan to the microphones is then influenced by the reflection and shadowing by the housing of the heat exchanger. This is shown schematically in Fig. 1(c).

If in such cases beamforming is done based on free field Green's functions, the disturbance of real sound path leads to insufficient beamfoming results in the lower frequency range, where the outer (in this case shadowed) microphones are required for a sufficient source localization. The aim of the present work is to develop a method to calculate the Green's functions for typical fan installation conditions and to use these tailored Green's functions in the calculation of the beamforming steering vectors. The Green's functions are calculated in the stationary reference frame and the hence derived steering vectors are used for both stationary and rotating beamforming. The stationary reference frame calculations used here are based on the assumption that the air flow and the convective amplification can be neglected. Sarradj et al. [12] have shown that the influence of the intake flow on the sound propagation can be neglected for a slow moving fan (tip speed $< 0.15\,\mathrm{Ma}$).

In the following, an overview of beamforming methods under disturbed sound propagation will be given. So far these methods have been mainly investigated for closed test sections of wind tunnels.

The first published method is the Image Source Method (ISM) by Guidati et al. [13]. The positions of reflected mirror sources are determined numerically and taken into account in the steering vectors. The damping of each mirror source was determined experimentally by measurements in the reverberant environment of a closed test section. Using the same idea, Fischer & Doolan [14] presented two methods, numerically and experimentally, to involve the reflections in beamforming in closed test sections. The numerical method is also based on Green's functions with mirror sources according to the wind tunnel wall reflections. The second method measured the Green's functions with a generic source inside the closed test section at the focus grid points. The source localization was mostly improved when using the experimental Green's functions, especially at high frequencies. The best results were obtained when using the experimentally determined Green's functions combined with CLEAN-SC.

In [15], Sijtsma and Holthusen have presented an approach in which the beamformer output is minimized for the directions of the mirror sources. They added a control mechanism to preserve robustness especially at low frequencies. This method succeeded well in reconstructing source levels in the entire frequency range investigated in the paper. Below $f = 2500$ Hz however, the position of the maximum in the beamforming map deviates significantly from the actual source position.

Another approach was published by Fischer & Doolan [16]. They identified the mirror sources by means of different time delays in the cross-correlation matrix (CCM) and removed their influence by multiplying each CCM vector by a window function centred at the main peak. The cross-correlation matrix is derived from the cross-spectral matrix. An advantage of the method is that no information about the geometry of the reverberant environment is required. It could be shown that the beamforming maps in a reverberant test section could be improved for a loudspeaker without flow as well as for an aerofoil in a flow. The beamforming results for the loudspeaker were comparable with the theoretical Point Spread Function of the array.

Bousabaa [17] presented a method to determine the Green's functions numerically in the time domain. Using a single aeroacoustic CAA simulation, the Green's functions are calculated from all focus points to all microphones. Therefore, both flow and diffracting objects are taken into account in wind tunnel measurements. The method takes advantage of the sparsity of Green's functions for these cases. Therefore, only external aeroacoustic problems can be modelled, because in other cases the Green's functions are not sparse enough. The method is therefore only suitable for non-reflective measurement environments.

A further simulation-based approach is presented by Kaltenbacher et al. [18]. Here, first the acoustic wave equation is solved using the Finite Element Method (FEM). In doing so, the actual boundary conditions of the given measurement setup can be considered. Second, the inverse problem is solved to match both, the measured and simulated pressure. The goal is to consider acoustic problems in the low frequency range. In numerical 2D and 3D setups it can be shown that the method improves sound source localization at low frequencies [18,19]. Additionally, in [20], the Green's functions from the FEM have been used directly to calculate the steering vectors for numerical beamforming. This use of numerically calculated steering vectors improved the results

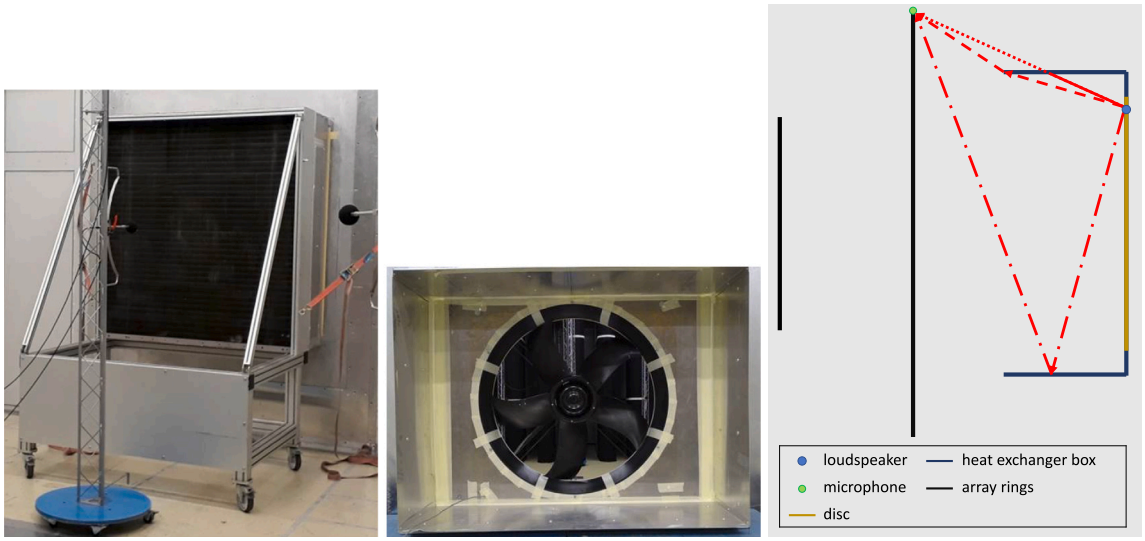

Fig. 1. Example of a fan mounted in a heat exchanger. (a): Suction side view of a heat exchanger. (b): Suction side view of an axial fan in a heat exchanger housing without condenser. (c): Impact of the heat exchanger box on sound propagation from source to array microphones. The dimensions of this setup up are given in Section 2.5.1.

compared to beamforming maps with free-field steering vectors as well. The calculation of Green's functions is done reciprocal, i.e. from the microphones to the focus points. Thus, the number of simulations to be run corresponds to the number of microphones.

Most of the presented methods have been developed for closed test sections in wind tunnels and therefore only consider reflections. The method of Bousabaa however, has been developed for non-reflective environments. For the presented fan application with heat exchanger, the Green's functions includes reflection, diffraction and shadowing effects. This is necessary to use a microphone array whose aperture is larger than the cross section of the heat exchanger. The method of Kaltenbacher determines the complete Green's functions by FEM simulations. However, its applicability has so far been shown only for numerical cases. Furthermore, none of these methods consider moving sound sources.

In the present work numerical simulations are used to calculate the transfer functions between monopoles at the microphone positions and the beamforming focus grid points (i.e. the possible position of the acoustic sources). The resulting Green's functions are used to calculate so-called 'tailored' steering vectors to perform beamforming in the frequency- and time-domain using experimental measurement data. The simulations of the transfer functions are done in the frequency domain using the Boundary Element Method (BEM) in a stationary reference frame. The Green's functions consider the effects of reflection, diffraction and shadowing of the heat exchanger but the method can by applied for arbitrary geometries.

The investigations in this paper are done for a stationary and a rotating measurement setup using a generic loudspeaker source. Beamforming is also performed in both stationary and rotating reference frame. In the stationary case, beamforming is done in frequency domain using steering vectors based on the tailored Green's functions. For the rotating case, in a first step the BEM-simulation based stationary tailored steering vectors are transformed from frequency to time domain. Then a generalized beamforming method in time domain is presented where these tailored steering vectors are used for rotating time domain beamforming. This generalized time domain beamformer also includes the weighting of the tailored Green's functions to calculate the corresponding steering vectors.

The aim of the work is to investigate how far the beamforming results are degraded by the reflection and shadowing of the heat exchanger housing, when using free-field steering vectors. Furthermore, it will be analysed to what extend this reflection and shadowing can be compensated by the usage of simulated, tailored Green's functions for beamforming of real measurement microphone data. The qualitative improvement of the beamforming maps, especially in terms of main lobe width and the presence and strength of side lobes, will be considered. The estimation of the absolute source power is not in the scope of the study.

The paper is organized as follows: First, in Section 2 the beamforming formulations are presented. Then, criteria for the evaluation of the beamforming results are introduced and the investigated test case is presented. In Section 3 the beamforming results are presented and discussed. The work is summarized in Section 4.

2. Methods

In the following chapter the basics for the application of the beamfoming with BEM simulated Green's functions will be given. First of all, an overview of the necessary mathematical formulations of beamforming using numerically calculated Green's functions is given. Afterwards, different validation criteria for the evaluation of the beamforming results are introduced. Lastly, the experimental test case selected for validation is presented.

2.1. Beamforming

Beamforming of phased microphone array measurements is a technique for sound source localization and the estimation of the according source power. Therefore, given focus points are scanned at locations where possible sound sources are expected. This is done by manipulating the microphone signals for each focus point according to the steering vectors, which describe the sound propagation between the focus points and each microphone position. Afterwards, all microphone signals are summed up and the result is recorded in a source map. This source map is often called *dirty map*, because it includes all the influences of the used microphone array and steering vectors. Often, this *dirty map* is *cleaned* using further methods called *deconvolution* methods. These deconvolution methods are however not in the focus of this paper.

The beamforming procedure can be performed either in the time domain or in the frequency domain. In the following, frequency domain beamforming for stationary test cases is presented first. This is done based on [21]. Afterwards it will be shown how the tailored Green's functions from BEM simulations can also be used for rotating beamforming. Therefore, the transformation of the tailored Green's functions from frequency to time domain will be discussed first. Then the corresponding rotating beamforming algorithm is presented.

2.1.1. Frequency domain beamforming using cross spectra

A common approach is to apply beamforming to the microphone signals in the frequency domain. A computationally fast approach to this is to separate the processing of the microphone data from the calculation of the sound propagation information. This way, only one transformation of the microphone signals to the frequency domain has to be performed. The propagation from every possible chosen source position to each microphone is performed separately. The complex pressure amplitudes $\hat{p}_m(f)$ of the microphone signals can be calculated by a discrete Fourier transformation for a block of K samples:

$$\hat{p}_m(f) = \frac{2}{K}\sum_{k=1}^{K} p_{m,k} e^{-2\pi i f k \Delta t}. \tag{1}$$

To estimate the degree of correlation between two microphone signals, the cross power is calculated:

$$C_{mn}(f) = \mathrm{E}\left(\frac{1}{2}\hat{p}_m(f)\hat{p}_n^*(f)\right). \tag{2}$$

where $*$ indicates the conjugate complex and E(.) the expected value. This is done using Welch's method [22]. In the following the dependency on the frequency f is mostly omitted to increase the readability. The auto- and cross-powers of all microphone signals are stored in the cross-spectral matrix (CSM) $\mathbf{C}$:

$$\mathbf{C} = \mathrm{E}\left(\frac{1}{2}\hat{\mathbf{p}}\hat{\mathbf{p}}^*\right) \in \mathbb{C}^{M\times M}, \tag{3}$$

with the M-dimensional vector $\hat{\mathbf{p}}$ of complex pressure amplitudes:

$$\hat{\mathbf{p}} = \begin{pmatrix} \hat{p}_1(f) \\ . \\ . \\ . \\ \hat{p}_M(f) \end{pmatrix} \tag{4}$$

For the estimation of the source power at a certain focus point, information about the transfer function or Green's function $\hat{g}(\mathbf{x},\mathbf{y})$

$$\hat{g} : \mathbb{R}^3 \times \mathbb{R}^3 \to \mathbb{C} \tag{5}$$

from the focus point position $\mathbf{y} \in \mathbb{R}^3$ to the microphone position $\mathbf{x} \in \mathbb{R}^3$ is needed. This information is stored in the vector of the Green's functions $\hat{\mathbf{g}} = \hat{\mathbf{g}}(\mathbf{y}) \in \mathbb{C}^M$, where $\hat{g}_m = \hat{g}_m(\mathbf{y}) = \hat{g}(\mathbf{x}_m, \mathbf{y})$ and $\mathbf{x}_m \in \mathbb{R}^3$ is the position of the mth microphone. Its components are the pressure amplitudes induced by a unit sound source at the focus point in dependence of the source model and the radiation conditions. For a monopole source and free-field conditions, $\hat{g}_m$ for a certain microphone m can be written as follows:

$$\hat{g}_m = \frac{1}{r_m}\mathrm{e}^{-jkr_m}, \quad r_m = \|\mathbf{y} - \mathbf{x}_m\|_2, \tag{6}$$

where r_m is the distance between the focus point $\mathbf{y}$ and the mth microphone position $\mathbf{x}_m$. In this paper, the Green's functions $\hat{g}_m$ for the measurement setup are calculated numerically by boundary element simulations.

To estimate the source auto-power at a certain focus point one has to evaluate:

$$A = \hat{\mathbf{w}}^*\mathbf{C}\hat{\mathbf{w}} \tag{7}$$

where $\hat{\mathbf{w}}$ is the so called steering vector, which is defined in the next section.

2.1.2. Steering vector formulations

There are several possible formulations for the steering vector $\hat{\mathbf{w}} = \hat{\mathbf{w}}(\mathbf{y}) \in \mathbb{C}^M$. An overview of the most frequently used is given by Sarradj in [23]. In this work, formulation three according to [23] is applied on analytical free-field and on numerically computed arbitrary Green's functions. It is based on the minimization of the difference between the measured pressure vector and the product of the complex source amplitudes and the Green's functions (see [21], Eq. (45)). The resulting steering vector formulation reconstructs the source power correctly, but not the source position at a local maximum of the beamforming map:

$$\hat{w}_m = \frac{\hat{g}_m}{\|\hat{\mathbf{g}}\|_2^2} \tag{8}$$

In the special case of a free field without flow Green's function (Eq. (6)) the steering vector formulations is:

$$\hat{w}_m = \mathrm{e}^{-jkr_m} \frac{1}{r_m} \frac{1}{\sum_m r_m^{-2}} \tag{9}$$

2.1.3. Point spread function

The point spread function is the spatial impulse response of an array on a unit point source at a focus point $\mathbf{y}_s$. As it induces a CSM by

$$\mathbf{C}_s = \hat{\mathbf{g}}(\mathbf{y}_s)\hat{\mathbf{g}}(\mathbf{y}_s)^* \tag{10}$$

the source power can be calculated as follows:

$$A^{\mathrm{PSF}}(\mathbf{y}) = \hat{\mathbf{w}}(\mathbf{y})^* \mathbf{C}_s \hat{\mathbf{w}}(\mathbf{y}) = \hat{\mathbf{w}}(\mathbf{y})^* \hat{\mathbf{g}}(\mathbf{y}_s)\hat{\mathbf{g}}(\mathbf{y}_s)^* \hat{\mathbf{w}}(\mathbf{y}) = \left|\hat{\mathbf{w}}(\mathbf{y})^* \hat{\mathbf{g}}(\mathbf{y}_s)\right| \tag{11}$$

2.2. Green'S functions from boundary element method simulations for steering vector calculation

In this paper the Green's functions are calculated with the boundary element method (BEM) in the frequency domain. The simulation setup will be described in Section 2.5.2. The calculation is done reciprocal which means that the scattering problem of a delta function δ located at the microphone position $\mathbf{x}_m$ is solved for each microphone:

$$\hat{g}_m^{\mathrm{BEM}}(\mathbf{y}) = \hat{g}(\mathbf{y}, \mathbf{x}_m) \tag{12}$$

Due to the known reciprocal property of the wave equation without flow and arbitrary boundary conditions [24], this is the same as calculating the Green's function from the focus point $\mathbf{y}$ to the microphone position $\mathbf{x}_m$:

$$\hat{g}(\mathbf{y}, \mathbf{x}_m) = \hat{g}(\mathbf{x}_m, \mathbf{y}) \tag{13}$$

The solution is evaluated at the focus points $\mathbf{y}$ of the beamforming map. The resulting complex pressure amplitudes can be used directly as Green's functions $\hat{g}_m$ in the steering vector formulation (Eq. (8)) for frequency domain beamforming.

2.3. Rotating beamforming with steering vectors from tailored Green's functions

As already discussed in the introduction, for the rotating setup the beamforming has to be performed in the time domain. This is because the setup is not rotationally symmetric and therefore the tailored Green's functions become time dependent.

2.3.1. Transformation of the steering vectors into the time domain

To run the beamforming in the time domain, the steering vectors are transformed into the time domain first. Therefore, BEM simulations are carried out for multiple frequencies in a certain range $f_{\mathrm{min}}^{\mathrm{BEM}} \leq f^{\mathrm{BEM}} \leq f_{\mathrm{max}}^{\mathrm{BEM}}$. The difference between two simulated frequencies is Δf^{BEM}. From the resulting tailored Green's functions $\hat{g}_m^{\mathrm{BEM}}(f)$ the steering vectors $\hat{w}_m^{\mathrm{BEM}}(f)$ are computed according to Eq. (8) for each frequency f^{BEM}. If the maximum simulated frequency $f_{\mathrm{max}}^{\mathrm{BEM}}$ is lower than half of the sampling rate of the measurement f_s, the remaining frequency entries in the steering vector spectrum are set to zero. Then the spectrum of the steering vectors is transformed from frequency into time domain by inverse fast fourier transform (iFFT). To determine the negative frequencies, it is conjugate complex mirrored first.

$$w_m(t) = \mathcal{F}^{-1}\hat{w}_m(f) \tag{14}$$

with $-f_s/2 < f < f_s/2$. The resulting impulse response in time domain consist of $N_{\mathrm{sw}} = f_s/\Delta f^{\mathrm{BEM}} + 1$ samples.

2.3.2. Beamforming

The time signals of the focus points $\bar{\sigma}(t, \mathbf{y}(t))$ are generated time step by time step from the measured microphone signals. For each time step the microphone signals are multiplied by the corresponding impulse responses and the resulting time signal is summed up. For a stationary focus grid this corresponds to a convolution of the microphone signals p_m with the corresponding impulse response $w_m(t, \mathbf{y})$ from the microphones m to the (static) focus positions $\mathbf{y}(t) = \mathbf{y}$.

$$\bar{\sigma}(t, \mathbf{y}) = \frac{1}{M} \sum_{m=1}^{M} \left(p_m * w_m(\mathbf{y}) \right)(t) \tag{15}$$

A co-rotating focus grid is used to evaluate the rotating measurements. This makes the steering vectors dependent on time t. To determine the impulse response $w_m(\hat{t}, \mathbf{y}(t))$ at a certain time t, spatial interpolation is required. $\hat{t}$ describes the relative time of the impulse response and is different from the global time t. For the time t considered, the position $y(t)$ of the rotated focus grid point is calculated and the impulse response $w_m(\hat{t}, \mathbf{y}(t))$ at time t is determined by spatial nearest neighbour interpolation in the simulated BEM data. In other words, the simulated BEM impulse responses are used as a look-up table using nearest neighbour interpolation.

The microphone signals can no longer be convolved with the impulse response, due to the movement of the focus positions. Instead, for each time t the corresponding sections from the microphone signals $p_m(t+n\Delta t)$ have to be multiplied with focus position $\mathbf{y}(t)$ dependent impulse response $w_m(\hat{t}, \mathbf{y}(t))$.

$$\bar{\sigma}(t, \mathbf{y}(t)) = \frac{1}{M} \sum_{m=1}^{M} \sum_{n=0}^{N_{\mathrm{sw}}-1} p_m(t + n\Delta t)\, w_m\left((N_{\mathrm{sw}} - n - 1)\Delta t, \mathbf{y}(t)\right) \tag{16}$$

with $\Delta t = \frac{1}{f_s}$, f_s the sampling frequency and N_{sw} the number of time samples in the BEM impulse response.

The Doppler shift, which is caused by the source and receiver being in different reference systems, is corrected automatically because in the present method the evaluation of the rotating sources take places in the co-rotating focus-grid reference frame $\mathbf{y}_{\mathrm{rot}}$.

However, convective amplification due to the movement of the sound sources is not taken into account. Any kind of interpolation in the time domain of the microphone signals $p_m(t)$ is not required when following the approach shown in Eq. (16).

2.4. Validation criteria

The beamforming results for the stationary and the rotating test cases will be compared in the next section. Therefore, four different validation criteria are now established as measure of the resulting beamforming maps. It shall be mentioned again that all criteria are based on so-called 'dirty maps' on identical grids without further deconvolution methods. These criteria shall express different properties of the beamforming maps in single values. They aim at two aspects: The first aspect evaluates the calculation of the sound power of the source. The second aspect evaluates how other sources are masked by a broad main lobe or side lobes of the point spread function.

The definition of the first criterion is based on Sarradj [23] and aims at the power of the sound source: The beamformer output at the source position should be a measure of the **source power**, as the difference between the indicated source power A_e and the true source power A_s

$$\Delta L = A_e - A_s. \tag{17}$$

Because the true source power is not known for the given measurement setup in this paper, the true source power A_s is replaced by the indicated source power from a measurement without the heat exchanger box.

The second major aspect of the validation – the masking of other sources by the point spread function – will be based on the second and third criterion. The second criterion is the **main lobe width** b. It is a measure of how large the distance between two sound sources must be in order to be separated by the beamformer. It is calculated as twice the distance between the position of the maximum $\mathbf{y}_{\max}$ and the point on the $L_{\max} - 3\,\mathrm{dB}$ contour line most distant from the maximum.

$$b = 2 \cdot \max_{\hat{\mathbf{y}} \in S} \left(||\mathbf{y}_{\max} - \hat{\mathbf{y}}|| \right), \quad S = \{\mathbf{y} | L_{\max} - 3 = \mathrm{dB}(A(\mathbf{y}))\} \tag{18}$$

The third criterion is the **main lobe to side lobe ratio (MSR)**. It is also often referred to as dynamic range. In this paper it is calculated as the difference between the maximum level $L_{\max}$ and the level of the highest side lobe L_{SL}:

$$\mathrm{MSR} = L_{\max} - L_{\mathrm{SL}} \tag{19}$$

The highest side lobe is determined iteratively: Starting from the maximum of the beamforming map, the level is incrementally reduced. At each iteration the corresponding isolines are drawn into the map. At first, only the area of the main lobe is found. As soon as another area outside the main lobe is found, the highest side lobe is assumed there.

The fourth and final criterion, the **source to pattern ratio (SPR)**, addresses both aspects. It takes into account that not only the level of the highest side lobe, but the total energy added to the map by the point spread function is important for the quality of the results. Therefore, it is defined as the level of the ratio between the beamformer output at the source position and the average output at the other focus points:

$$\mathrm{SPR} = 10 \log_{10} \left(\frac{A(\mathbf{y}_s)}{\frac{1}{N_{\mathrm{map}}} \sum_{n=1}^{N_{\mathrm{map}}} A(\mathbf{y}_n)} \right) \tag{20}$$

where $\mathbf{y}_n$ is the nth focus point.

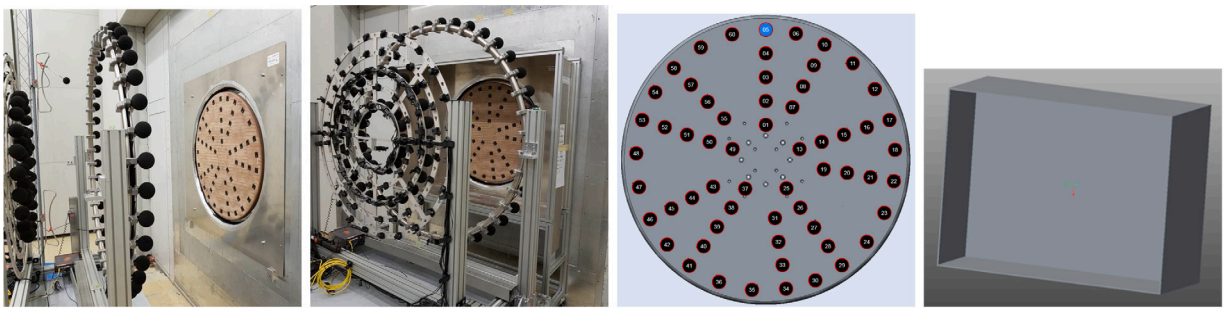

(a) (b) (c) (d)

Fig. 2. Validation setup. Side view of the measurement setup (a): without heat exchanger box and (b): with heat exchanger box. (c): Source position. (d): Simulation setup.

2.5. Validation setup

The following section will describe the setup that is used to validate the method. First the measurement setup and then its implementation in the BEM simulation will be presented.

2.5.1. Measurement setup

The goal of the presented method is to improve *dirty map*- beamforming results for sound source localization of axial fans mounted in heat exchangers. A simplified setup is shown in Fig. 2: The heat exchanger is modelled as a cuboid box without condenser.

A circular disc equipped with 60 loudspeakers is used as reference sound source (Fig. 2(c)). The disc is mounted on an electric motor so that it can be measured both stationary and rotating. The diameter of the disc is $d = 0.953\,\mathrm{m}$. For the present study, measurements results are shown where loudspeaker no. 5 (radius $r = 0.43\,\mathrm{m}$) is the sound source. The measurement signal is white noise in the frequency range $500\ \mathrm{Hz} < f < 10000\ \mathrm{Hz}$. Tonal sound sources have not been investigated in this paper. The sound power of the loudspeaker is not known. For this reason, the source levels of the various beamforming methods are compared relatively with those from a measurement without heat exchanger box (Fig. 2(a)).

The ebm-papst testbench for combined air and sound measurements is used for the validation experiments. It consists of two half-anechoic chambers separated by a wall where usually the fan is mounted in a so-called wall ring. The circular disc is flush mounted with the separating wall in the wall ring. The cuboid heat exchanger box is arranged concentric with the wall ring. It is connected to the wall and has the dimensions $1.54 \times 1.14 \times 0.46\,\mathrm{m}^3$.

The microphone array is arranged in two circles with $d_1 = 1.6\,\mathrm{m}$ and $d_2 = 0.8\,\mathrm{m}$ diameter. The larger circle houses $M = 40$ and the smaller circle $M = 24$ microphones. It is also arranged concentric with the wall ring. The distance from the separating wall to the larger microphone array circle is $z = 0.8\,\mathrm{m}$ and $z = 1.3\,\mathrm{m}$ to the smaller circle. A scaled sketch of the setup can be found in Fig. 1(c).

The data acquisition system is an I^2S- frontend by CAE Software and Systems GmbH with the corresponding digital MEMS microphones. The signals are recorded for 15 s, with sampling rate $f_S = 48077\ \mathrm{Hz}$. The microphone signals are resampled to $f_S = 24000\ \mathrm{Hz}$ to speed up the time domain beamforming algorithm. This is done in the time domain using the MATLAB function resample. It applies an antialiasing FIR lowpass filter, compensates its delay and interpolates the signal linearly at the new sampling rate.

To ensure that the frequencies in the CSM match the ones of the simulated, tailored Green's functions, a window size of $L = 401$ samples is used to achieve a frequency spacing of $\Delta f = 60\ \mathrm{Hz}$. The total number of $N = 1790$ averages is achieved using an overlap factor of $r = 0.5$. The procedure results in a matrix C for every bin centre frequency of the Welch estimation.

2.5.2. Simulation setup

The Green's functions are computed numerically with the Fast Multipole-Boundary Element Method (FM-BEM) code FMCAS [25, 26]. FMCAS solves the Helmholtz equation using a boundary integral equation discretized on a triangulated surface. The function to be determined is assumed to be constant on each triangle. The resulting system of linear equations is solved using an iterative solver from the PETSc library. The computation of the matrix–vector products is accelerated by a high-frequency Fast Multipole Method (FMM) based on a plane wave approximation. Further details of FMCAS can be found in the references cited above.

In the simulations only the heat exchanger box, the separating wall and the disc are considered. The disc and the wall are handled as a continuous surface. All surfaces are modelled fully reflective. A CAD model is shown in Fig. 2(d).

The cell size of the simulation grid is determined as a function of the simulated frequency. Above $f = 800\ \mathrm{Hz}$ grids with 12 points per wavelength (ppw) are used. In a preliminary study [27] it was shown that below $f = 800\ \mathrm{Hz}$ this is not sufficient to resolve the geometry properly. Therefore, the frequency dependent cell size is halved to 24 ppw.

Simulations are carried out for frequencies between $f_{\text{min}}^{\text{BEM}} = 60$ Hz and $f_{\text{max}}^{\text{BEM}} = 4500$ Hz. The distance between two frequencies is $\Delta f^{\text{BEM}} = 60$ Hz. For steering vector computation in time domain via iFFT, the entries in the steering vector spectra between $f_{\text{max}}^{\text{BEM}} = 4500$ Hz and $f_S/2 = 12000$ Hz are set to zero.

The Green's functions are evaluated on a square grid on the separating wall ($z = 0\,\text{m}$). It has the dimensions $1.44 \times 1.44\,\text{m}^2$. The distance between two evaluation points is $\Delta x = \Delta y = 0.01\,\text{m}$. This grid is also used as focus grid for the beamforming evaluations.

3. Results

In the following chapter, the method of tailored Green's functions will be used for beamforming on the presented measurement setup. Microphone array measurements were conducted with a loudspeaker mounted in a disc as a generic sound source as described in Section 2.5.1. The beamforming results are calculated in the frequency domain for the stationary setup and in the time domain for the rotating setup. Three different cases are considered for each setup, respectively: The first case is a measurement without the heat exchanger box and the steering vectors of the corresponding beamforming results are calculated based on the free-field Green's function (Eq. (6)). This first case will serve as a reference to show how the microphone array performs in the given test bench without the disturbance from the heat exchanger box. In the second case, microphone array measurements are performed in the same setup but with the heat exchanger box included in the measurements while the steering vectors are again calculated based on the free-field Green's functions. This case demonstrates the effects of the reflections and shadowing of the heat exchanger box on the beamforming results (using standard free-field based steering vectors). In the third case, the same array measurements with heat exchanger box are used, but this time the tailored steering vectors calculated on the basis of the BEM-simulated Green's functions are used for the evaluation of the beamforming results.

Firstly, the results for the stationary setup are presented followed by the results for the rotating setup in the subsequent subsection. In each case, the beamforming maps are shown first, followed by the validation criteria applied on the beamforming results, respectively. The results will be summarized in Section 3.3.

3.1. Results from stationary measurements

In this section, the results for the stationary measurement setup will be presented. The steering vectors of the beamforming maps are calculated on the basis of free-field or BEM-simulated Green's functions with reflections and shadowing, respectively. The beamforming maps are subsequently calculated using Eq. (7).

The beamforming maps for the three different cases are shown in Fig. 3(a). In Figs. 3(b)–3(e), the quality of the beamforming maps is evaluated using the four validation criteria from Section 2.4 as a function of frequency.

3.1.1. Beamforming maps

The beamforming maps for the three different stationary test cases are displayed in Fig. 3(a). The true source position which is known from the experimental setting, is marked with a cross. All beamforming maps of a certain frequency use the same colour map with dynamic range of 30dB. They are normalized with the frequency dependent maximum at each third octave band, respectively. This enables the direct comparison of the side lobes levels and main lobe width in the different cases relative to the third octave band maxima. On the other hand, with this representation of the beamforming results it is more difficult to compare the maxima and the ratio between the main lobe and side lobe levels within the different test setups. Therefore, Figs. 3(b)–3(e) show the validation criteria to ease the analysis of the maxima differences and main to side lobe ratio.

In the first row of Fig. 3(a) the beamforming maps of the measurement without heat exchanger box are shown, which have been evaluated based on free-field Green's functions. It can be seen that the main lobe is circular and becomes narrower with increasing frequency. Starting at $f = 800$ Hz, a strong circular side lobe can be seen that moves from the bottom of the maps towards the source position with increasing frequency. Its level is about 10 to 12 dB and therefore significantly higher than the levels at the focus points between this side lobe and the main lobe. From the frequency $f = 1250$ Hz on, further circular side lobes at similar levels appear between the described side lobe and the main lobe. The side lobes levels increase with frequency.

The second row of Fig. 3(a) shows the beamforming maps of the measurement with heat exchanger box, but again evaluated with free-field steering vectors. Especially at lower frequencies it can be seen that the main lobes are not longer circular but oval. As in the case without heat exchanger box, strong side lobes can also be observed. In the middle frequency range between $f = 1250$ Hz and $f = 2500$ Hz, these are more prominent than in the case without heat exchanger box. In addition, further side lobes can be seen that are not present in the results without the heat exchanger box. These are not circular and are located outside the circular side lobes.

The beamforming maps in the third row of Fig. 3(a) show the results for the measurements with heat exchanger box, but the beamfoming calculations use the tailored steering vectors, based on the Green's functions from BEM simulations as described in Section 2.5.2. The main lobe width appears smaller than in the maps of the first and second row. In addition, the side lobes are less visible and do not appear circular anymore. Instead, the side lobes have the shape of small spots. In the main, the side lobe levels appear reduced compared to the case above where the same measurement was evaluated with free-field steering vectors.

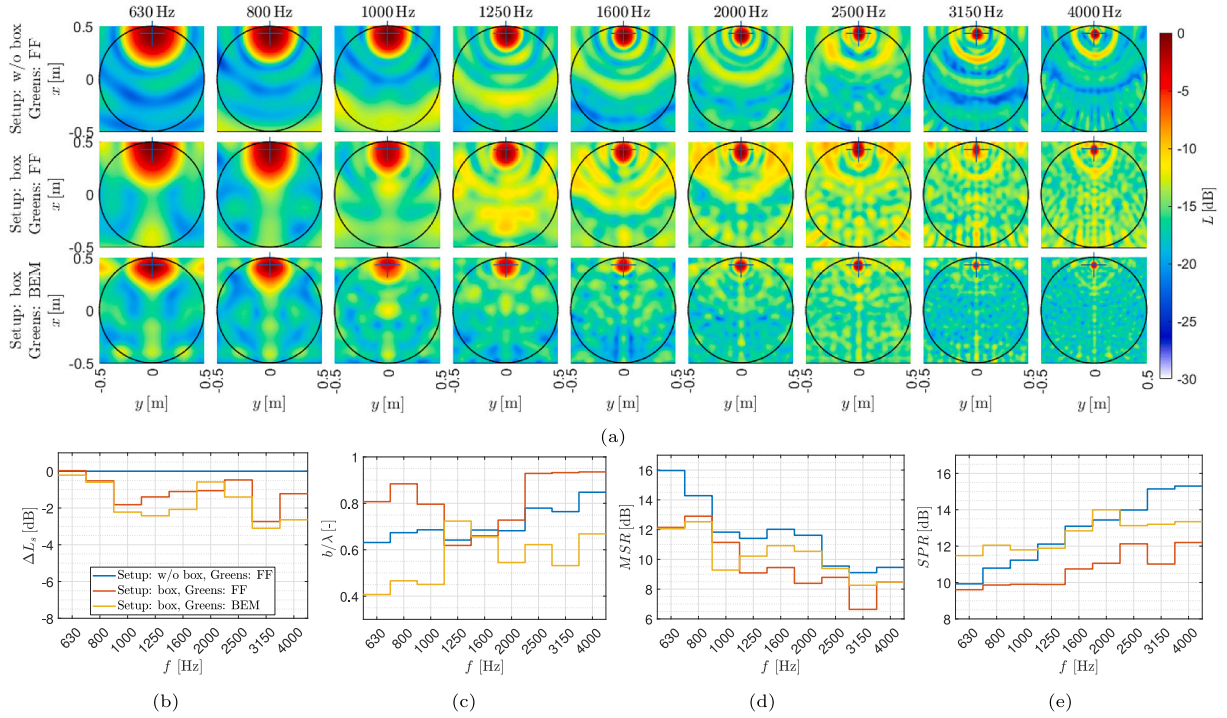

Fig. 3. Beamforming results from stationary measurements in one-third octave bands calculated with steering vectors based on free-field (FF) and BEM-calculated (BEM) tailored Green's functions.
(a): Beamforming maps with equal colour maps per frequency band. (b–e) Validation criteria: (b): Deviation from free-field source level, (c): Main lobe width, (d): Main lobe to side lobe ratio and (e): Source to pattern ratio.

3.1.2. Beamforming source level

The validation criteria shown in Figs. 3(b)–3(e) are related to the beamforming maps, respectively. In Fig. 3(b) the calculated beamforming levels at the source position are compared between the different test cases. The radiated sound power of the loudspeaker integrated in the test setup is not known and therefore cannot be used as reference. However, the level at the source position of the beamforming measurement without heat exchanger box is used as a reference with 0 dB at every third octave band. The beamforming levels at the source position of the measurements with heat exchanger box and free-field or tailored steering vectors are indicated as level difference to that reference, respectively.

From this evaluation it is not clear, whether the use of tailored Green's function can improve the determination of the source power. But as mentioned before, this is not in the focus of this paper.

For the measurement with the heat exchanger box installed, lower levels are found compared to the measurement without heat exchanger box at almost all frequencies. This holds for the beamforming calculations with free-field steering vectors as well as for those with tailored Green's steering vectors. Only at the lowest evaluated one-third octave band frequency $f = 630$ Hz the deviation for free-field beamforming is close to zero. The difference to the beamforming results with the tailored Green's steering vector is also very small with approximately $\Delta L_s = -0.2$ dB. The deviation increases with increasing frequency, for both test cases. The level difference for the beamformer with tailored steering vector is up to one decibel larger than for the free-field beamformer. In the upper middle frequency range, the level differences for both cases without heat exchanger box reduces again. Except for $f = 2000$ Hz, the level differences are always between 0.4 dB and 1.2 dB higher for tailored steering vector than for the free-field beamformer. In the two highest third octave bands the deviation increases again. At $f = 3150$ Hz it reaches the maximum of $\Delta L_s = -2.7$ dB and $\Delta L_s = -3.1$ dB, respectively.

The results shows that the installation of the heat exchanger box influences the levels of the beamforming maps at the source position. The use of numerically simulated tailored steering vectors cannot compensate for this influence. Instead, at the most frequencies the indicated source levels are further decreased when using the tailored steering vectors. This result is important to keep in mind while evaluating the criteria of the signal-to-noise ratio (Figs. 3(d) and 3(e)).

3.1.3. Main lobe width

Fig. 3(c) shows the main lobe width b of the beamforming maps for the three cases. The main lobe width b is normalized with the wavelength λ in order to clarify the dependency of the Helmholtz-number calculated this way. As mentioned in Section 2.4, the main lobe width is defined as the maximum spatial distance between the position of the maximum and the $L_{\max} - 3$ dB line.

The main lobe width of the beamforming maps based on the measurement without heat exchanger box and free-field steering vectors is approximately proportional to the wavelength for most frequencies. The ratio b/λ increases slightly from $b/\lambda = 0.62$ to $b/\lambda = 0.85$.

The normalized main lobe width generally widens for the measurement with heat exchanger box and free-field steering vectors. For the three lower and the three higher third octave bands it takes values between $0.8 < b/\lambda < 0.95$. In the three middle frequency bands ($1250\,\text{Hz} \leq f \leq 2000\,\text{Hz}$) the normalized main lobe width is in the range of the results without heat exchanger box for these frequencies ($0.6 < b/\lambda < 0.75$).

For the results based on Green's functions from BEM-simulations it is vice versa: In the three lower and four higher frequency bands, the main lobe width is reduced ($0.4 < b/\lambda < 0.7$). However, at $f = 1250$ Hz and $f = 1600$ Hz, it is in the same range as for the other two cases ($0.65 < b/\lambda < 0.75$).

The reduced main lobe width of the beamformer based on the tailored Green's functions at low frequencies can also be observed in the beamforming maps in Fig. 3(a). The main lobes of the beamfoming maps are significantly narrower when using the tailored steering vectors. The fact that their width at $f = 1250$ Hz and $f = 1600$ Hz is almost identical for all three cases, on the other hand, is not easily seen in the beamforming maps. The sizes of the red areas appear smaller in the bottom row. On closer inspection, however, it can be seen that the colour within these areas is more uniform than in those of the free-field beamforming maps. Thus, the spatial gradients from the maximum are smaller and the levels decrease only very slightly. Therefore, the considered $L_{\max} - 3\,\text{dB}$ region is relatively wide. If a larger threshold was chosen instead of $L_{\max} - 3\,\text{dB}$, the main lobe widths for the third case would also be found narrower compared to the free-field case at these frequencies.

Overall, the main lobe width appears significantly reduced by using the tailored Green's functions for the steering vector computation, especially when compared with the same measurements (with heat exchanger box installed). The decrease caused by the heat exchanger box in the results of the free-field beamformer is not only compensated for, the main lobe width is also reduced compared to the case of the free-field beamformer without heat exchanger box.

3.1.4. Main lobe to side lobe ratio

The third criterion, the main lobe to side lobe ratio (MSR), is displayed in Fig. 3(d). As mentioned before, only side lobes located in the area of the disc with the speakers have been considered in this criterion. The black circles in the beamforming maps in Fig. 3(a) mark these areas. It should also be noted that the MSR cannot be deduced directly as the level of the highest side lobe from the beamforming maps (Fig. 3(a)) due to fact that the colour maps of the three different cases are identical per third octave band frequency and thus the main lobe level differs (see Fig. 3(b)).

For the first case, where the measurement without heat exchanger box has been evaluated using free-field steering vectors, the MSR is highest in the two lower frequency bands $f = 630$ Hz and $f = 800$ Hz ($\text{MSR} \approx 16\,\text{dB}$ and $\text{MSR} \approx 14\,\text{dB}$). The reason has already been discussed when presenting the beamforming maps (Section 3.1.1); the main circular side lobe, which has a significantly higher level than the other side lobes, is still outside the evaluation area at these frequencies. In the frequency range starting at $f = 1000$ Hz, the MSR is controlled by the level of this side lobe. It can also be seen that the level of this side lobe increases in the upper frequency bands starting at $f = 2500$ Hz. From $f = 1000$ Hz to $f = 2500$ Hz the MSR is in the range $11\,\text{dB} < \text{MSR} < 12\,\text{dB}$. Above $f = 2500$ Hz the MSR reduces further to $9\,\text{dB} < \text{MSR} < 10\,\text{dB}$.

For the measurement with heat exchanger box, the MSR is reduced compared to the measurement without heat exchanger box by $\Delta\text{MSR} \approx 1\,\text{dB}$ to $\Delta\text{MSR} \approx 4\,\text{dB}$. By using tailored steering vectors for the evaluation of the measurements with heat exchanger, the MSR increases in the middle frequency range from $f = 1250$ Hz to $f = 3150$ Hz. For most frequencies, the MSR is in between the two results obtained with free-field steering vector. At $f = 2500$ Hz, the value of the measurement without heat exchanger box is even reached. In the lower frequency bands at $f = 630$ Hz and $f = 800$ Hz as well as in the highest frequency band $f = 4000$ Hz, the MSR levels for the two evaluations of the measurement with heat exchanger box are almost identical. Only at $f = 1000$ Hz the MSR of the evaluation based on tailored steering vectors is $\Delta\text{MSR} = 2\,\text{dB}$ lower than in the corresponding case with free-field steering vectors.

As explained, the disturbance of the sound propagation by the heat exchanger box causes an amplification of the side lobe already present in the case without heat exchanger box, especially in the middle frequency range from $f = 1250$ Hz to $f = 2000$ Hz. The resulting reduction in MSR can be reduced in this frequency range by using tailored Green's functions to calculate the steering vectors. This is true even though the main lobe appears at a lower source level in this case, which in principal has a negative effect on MSR.

3.1.5. Source to pattern ratio

The last criterion is the source to pattern ratio (SPR, Eq. (20)), which describes the logarithmic ratio between the sound pressure at the actual source position and the average sound pressure at all other focus points (within the evaluation area of the disc, indicated by the black circle). This criterion accounts for the effect that not only the highest side lobe has a negative effect on the sound source localization but any contribution to the beamforming map outside the source position. Furthermore, this criteria summarizes the other three criteria, the SPR increases due to high beamforming levels at the source position, it increases due to narrow the main lobe width and due to small side lobe levels.

The SPR for the three test cases are shown in Fig. 3(e). For the case without heat exchanger box, the SPR increases with the frequency. The levels are in the range $10\,\text{dB} < \text{SPR} < 15.5\,\text{dB}$. For the case with heat exchanger box and free-field steering vectors, the SPR is almost generally smaller than in the case without heat exchanger box. The difference increases with frequency due to

the fact, that SPR rises only in the range $9.5\,\mathrm{dB} < \mathrm{SPR} < 12.5\,\mathrm{dB}$. It is noticeable that the SPR between $f = 630$ Hz and $f = 1250$ Hz is $\mathrm{SPR} \approx 10\,\mathrm{dB}$ and only increases slightly above this range.

By calculating the steering vectors on the basis of the tailored Green's functions, the SPR is increased compared to the evaluation of the measurement with heat exchanger box using free-field steering vectors. Up to $f = 2000$ Hz, the values of the case without heat exchanger box are reached or even exceeded, especially for low frequencies ($f \leq 1000$ Hz).

This result shows that the quality of the beamforming results can be improved by using the tailored greens functions for the calculation of the steering vectors. Based on the evaluation of the criteria "main lobe width" and "MSR" it can be concluded that the improvement in the lower frequency range up to $f = 1000$ Hz is caused by the reduction on the main lobe width. In the middle frequency range between $f = 1250$ Hz and $f = 2000$ Hz it is caused by reduction of the highest side lobe level. The lower SPR compared to the test case without heat exchanger box in the frequency range above $f = 2000$ Hz is mostly caused by the lower source level of the main lobe.

3.1.6. Discussion and conclusions from stationary measurement results

In the previous subsection, the results for the stationary measurement have been presented in the form of beamforming maps and the corresponding validation criteria. This opens the discussion on two aspects: The influence of the reflections and shadowing of the heat exchanger box on the array measurements itself and to what extend this influence can be compensated by the use of numerically simulated tailored Green's functions for the calculation of the steering vectors.

We have seen, that both the main lobe width and the side lobe level increase for the evaluation with free field steering vectors if the heat exchanger box is present in the measurement, which reduces the MSR and SPR at all considered frequencies.

A possible explanation is related to the fact that some of the array microphones on the large array ring are geometrically shadowed by the heat exchanger box. The propagation time of the sound to these microphones is increased and deviates from the free-field conditions which leads to a broadening of the main lobe. Since the sound source is positioned at the upper area of the heat exchanger box, the upper microphones of the larger array ring are shadowed. When calculating the sound level at a certain focus point, the microphone signals are delayed according to the associated steering vector. However, for the upper microphones, the actual delay in the measurement setup does not match the free-field steering vector of the source position. Instead it matches the steering vectors of focus points more distant from the microphones. This conflicts with the unshadowed microphones and leads to the observed broadening of the main lobe, especially in the vertical direction. In the horizontal direction, the broadening is less visible because more microphones are not shadowed.

Another aspect is the influence of reflections. The sound emitted by the loudspeaker is reflected by the walls of the heat exchanger box and reaches the microphones not only on the direct path but also indirectly, via reflections. The reflected sound waves hit the array from different directions than the direct sound waves (leading to different phase differences at the array microphones) and are therefore interpreted by free-field steering vectors as additional sources. This increases the side lobes, too.

The validation criteria tested on the beamforming maps show that for the measurement with heat exchanger box the beamforming results can be significantly improved by using the BEM-simulated tailored Green's functions. The BEM-simulated Green's functions can improve the beamforming results in two ways: The reflected sound waves match the steering vectors, too and appear therefore not as additional sources in the beamforming maps. The side lobes are therefore decreased. Secondly, the beamforming algorithm is provided with even more (valid) information than in the first case without heat exchanger box and free-field steering vectors. The microphone array can be interpreted as virtually mirrored on the heat exchanger box walls, thus enlarging the aperture and reducing the main lobe width of the beamforming maps.

It is noticeable that the main lobe width reduces more in vertical direction than in horizontal direction. One possible explanation is that in the present case the large distance to the bottom wall and the corresponding clear reflections on this wall offers the beamforming algorithm more information and therefore increases the virtual mirrored array in the vertical direction. Another possible explanation for the reduced main lobe width is that the BEM-simulated Green's functions model the diffraction of the sound at the edges of the heat exchanger box, so that diffracted microphone signals match the correct propagation model in the beamforming process. This also would improve the beamforming results due to the larger aperture and increased number of useful microphone signals.

When presenting the results, it has also been shown that for the free-field beamformer the level at the source position is lowered for the measurement with the heat exchanger box. It can be assumed that the shadowing of some microphones in the measurement reduces the sound pressure more than predicted by the free-field steering vectors. The reduction of the levels at the source position cannot be compensated by using the BEM-simulated Green's functions to calculate the steering vectors. A possible explanation for this are that there are still deviations between the real wave propagation and the simulated Green's functions. Because the BEM-simulated Green's functions include reflection and diffraction they are much more sensitive to geometric inaccuracies. This can cause deviations in the calculation of amplitude as well as in the determination of phase of the sound propagation.

An overestimation of the amplitudes of the Green's functions by the BEM-simulations would lead to an underestimation of the source powers by the beamforming algorithm. The larger the amplitude of the Green's functions are, the smaller the amplitudes of the steering vectors become, because in the chosen steering vector formulation the Green's functions are weighted by their squared magnitude (Eq. (8)). According to Eq. (7), the smaller the magnitude of the steering vectors are, the smaller the predicted source powers become.

One possible reason for an incorrect determination of the amplitudes (and the phase) of the Green's function is related to reflections. In the simulations, total reflection at all frequencies is assumed at the walls of the heat exchanger box. However, it can be assumed that in the real measurement the sound is not only reflected but also absorbed at the walls of the heat exchanger

box depending on the frequency and angle of incidence. Thus, the reflections in the measurements are most probably smaller than in the BEM-simulation with the assumed total reflection.

Errors in the determination of the phase of the Green's function can also be caused by geometrical deviations between real measurement setup and simulation setup. If the distances between sound sources, microphones and geometrical objects do not match, deviations in the travel times would appear and cause errors in the phase shift of the measured microphone signals with the simulated steering vectors in Eq. (7). This mismatch of the phase would reduce the received source power in the beamforming map, too.

3.2. Results from rotating measurements

Following the results of the stationary measurements, the rotating measurements will be investigated in this section. The beamforming maps have been calculated as described in Section 2.3. The rotational speed in all test cases is $n = 230$ rpm. Again, the beamforming maps are presented first followed by the corresponding validation criteria. The discussion of the results follows at the end of the section.

3.2.1. Beamforming maps

The beamforming maps are shown in Fig. 4(a). The arrangement of the individual maps corresponds to that in Fig. 3(a), in the first row the measurement without heat exchanger box is shown, in the second row the measurement with heat exchanger box, both measurements evaluated with free-field steering vectors. The third row shows the results for the measurements with heat exchanger box, but the beamforming results evaluated the tailored steering vectors.

For the case without heat exchanger box (first row in Fig. 4(a)), the beamforming maps of the rotating measurement are similar to those of the stationary measurement (first row in Fig. 3(a)). This is true for the width of the main lobe as well as for the level and the position of the side lobes. One difference is that the maps are not so structured outside the main lobe at higher frequencies, the side lobes appears more smooth.

The results for the free-field beamforming of the measurement with heat exchanger box are similar. The numerous single side lobes that were found in the stationary case are no longer visible. Instead, the side lobes appears more in circular form. Outside of the first strong side lobe the sound power level of the beamforming map is spatial more evenly distributed. Its value corresponds to the averaged level of the respective area of the maps from the stationary measurement. The main lobes appear in this rotating case circular, in contrast to the oval shape of the main lobes at the stationary measurement.

In the third row, showing the maps of the measurement with heat exchanger box and steering vectors from tailored Green's functions, only slight circular side lobes can be seen. The beamforming maps outside of first side lobe are nearly constant, but at lower levels. The main lobes are again circular.

3.2.2. Beamforming source level

Firstly, beamforming levels at the source position are compared in Fig. 4(b). The stationary measurement without heat exchanger box is used as the reference case. The differences to the corresponding rotating test case without heat exchanger box (free-field Green's functions were used to calculate the steering vectors) do not exceed $\Delta L_s < 0.5$ dB.

The differences of the source levels between the measurement with and without heat exchanger box and evaluation with free-field steering vectors are smaller than in the corresponding stationary test cases. The level differences are in the range of $0.2\,\text{dB} < \Delta L_s < 1\,\text{dB}$ for all frequencies.

The differences between the measurements with heat exchanger box and steering vectors from tailored Green's functions are between $\Delta L \approx 0.5$ dB and $\Delta L \approx 4$ dB and therefore larger than between the stationary test cases. The frequency dependence is similar to the stationary case. Firstly, the level difference increases with the frequency, followed by an interval between $f = 1600$ Hz and $f = 3150$ Hz with a reduced difference. Above $f = 3150$ Hz the level difference increases again reaching the maximum at $f = 4000$ Hz.

3.2.3. Main lobe width

Fig. 4(c) compares the main lobe width for the three different rotating test cases. At the case without heat exchanger box and the beamforming calculations with free-field steering vectors the result is similar to the corresponding stationary case. The normalized main lobe width slowly increases with the frequency from $b/\lambda = 0.6$ to $b/\lambda = 0.85$.

Comparing the test case without heat exchanger box to the test case with heat exchanger box (both evaluated with free-field steering vectors) the normalized main lobe width appears higher for all frequency bands. However, the differences are smaller ($\Delta b/\lambda < 0.1$) than in the stationary case, especially at low and high frequencies.

By using tailored steering vectors to calculate the beamforming of the measurement with heat exchanger box the normalized main lobe width decreases for all frequencies compared to both test cases with free-field steering vectors. The largest improvements are achieved at $f = 2500$ Hz with $\Delta b/\lambda \approx 0.15$ and $\Delta b/\lambda \approx 0.225$ compared to the test cases without and with heat exchanger box, respectively.

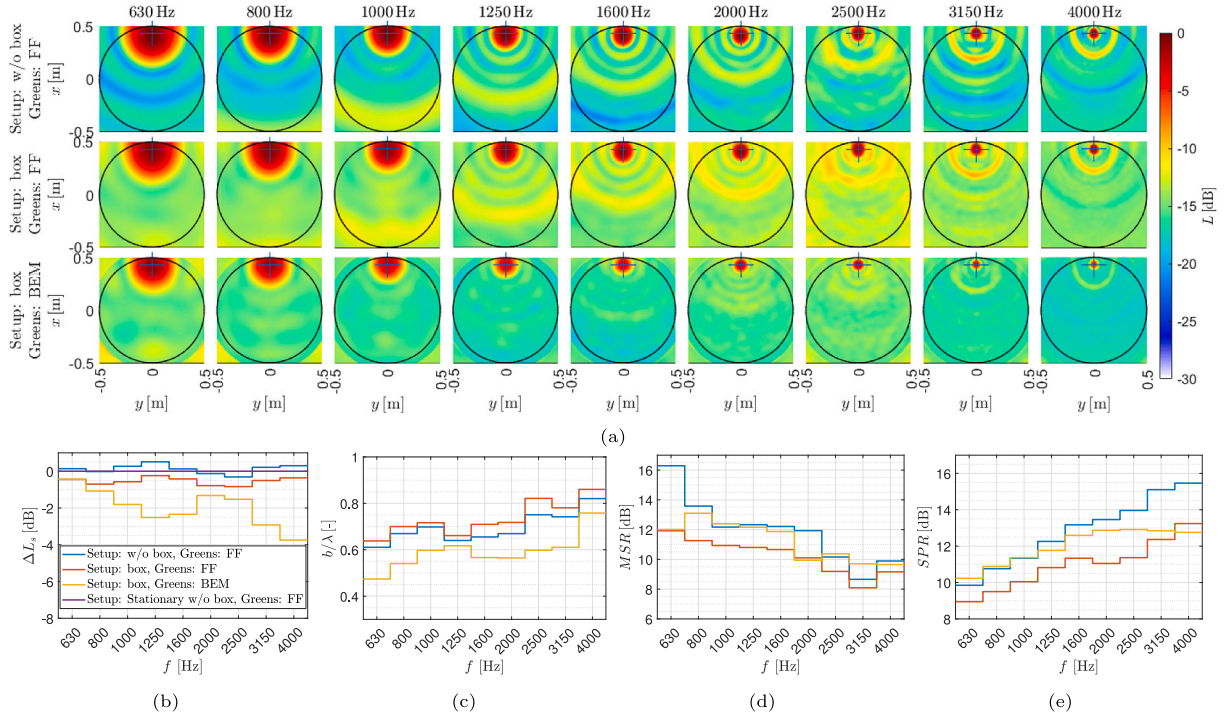

Fig. 4. Beamforming results from rotating measurements in one-third octave bands calculated with steering vectors based on free-field (FF) and BEM-calculated (BEM) tailored Green's functions.
(a): Beamforming maps with equal colour maps per frequency band. (b–e) Validation criteria: (b): Deviation from free-field source level, (c): Main lobe width, (d): Main lobe to side lobe ratio and (e): Source to pattern ratio.

3.2.4. Main lobe to side lobe ratio

The main lobe to side lobe ratio for the three rotating test cases is shown in Fig. 4(d). Again, only focus points within the black circle (on the rotating disc) are considered. The MSR for the case without heat exchanger box and free-field steering vectors appears similar to the corresponding stationary case.

MSR reduces when evaluating the rotating measurement data with heat exchanger box and free-field steering vectors. However, for the most frequencies the differences are smaller than in the stationary case.

The MSR for the beamforming of the measurement with heat exchanger box using the tailored steering vectors increases again, reaching or even slightly exceeding the MSR of the measurement without heat exchanger box.

3.2.5. Source to pattern ratio

The SPR for the rotating case is shown in Fig. 4(e). Again, only focus points on the rotating disc have been considered for the calculation.

For the rotating measurement without heat exchanger box and beamforming with free-field steering vectors the SPR is almost identical to that of the corresponding stationary case.

In the case of the measurement with heat exchanger box and beamforming with free-field steering vectors, the SPR is reduced by $1\,\text{dB} < \Delta\text{SPR} < 3\,\text{dB}$ compared to the test case without heat exchanger box.

By using tailored Green's functions the SPR increases again reaching the SPR level of the measurement without heat exchanger box in the three lower one-third octave band ($f = 630$ Hz to $f = 1000$ Hz). In the one-third octave bands from $f = 1250$ Hz to $f = 3150$ Hz the SPR is increased compared to the measurement with heat exchanger box and evaluation with free-field steering vectors. However, the SPR values of the measurement without heat exchanger box are not reached. Only in the one-third octave band $f = 4000$ Hz the SPR for the measurement with heat exchanger box is lower ($\Delta\text{SPR} \approx 0.5\,\text{dB}$) when using the tailored steering vectors instead of the free-field steering vectors.

3.2.6. Discussion and conclusions from rotating measurement results

In the following, the results of the rotating beamforming will be summarized and discussed. The results in the previous subsection show, that also in the rotating cases the beamforming results are degraded by the influence of the heat exchanger box. However, the differences in the different validation criteria are for most frequencies smaller compared to the stationary measurements. Furthermore, the deviations are not as frequency dependent as in the stationary cases.

The beamforming results with steering vectors based on the tailored Green's functions are generally improved. In many cases the level of the measurement without heat exchanger box is reached or even exceeded. The improvement is more independent of the frequency than in the equivalent stationary cases. However, the deviations of the level at the source position are larger than in the stationary case. Furthermore, a clear dependence on the frequency can be seen in this criterion.

These results indicate, that the actual acoustic boundary conditions of the given rotating measurement setup can be determined with sufficient accuracy by the implemented BEM-simulations for the given rotating measurement setup. The implementation of the generalized time domain beamformer which enables the use of the tailored Green's functions in the steering vectors improved the main lobe width and suppression of the side lobes also for the rotating test case. It could be observed that the improvement of the beamforming results depends less on the frequency than in the stationary case. We can assume that the source rotation leads to a circumferential averaging of position-dependent effects so the improvement in the rotating test cases are even more important than in the stationary test cases.

The differences between the source levels appear frequency-dependent but not compensated by circumferential averaging.

3.3. Summary of the results

In this paper, four different validation criteria are introduced as measures to compare different beamforming maps. These validation criteria were applied to beamforming maps that are set up using three different test cases in stationary and rotating reference frame, respectively.

The Greens's functions were calculated (stationary) in the frequency domain between the microphone positions and the focus grid behind a heat exchanger box using BEM-simulations. Only the housing of the heat exchanger has been taken into account. It has been modelled as a box with a rectangular shape. The BEM simulated – tailored – Green's functions were afterwards used to calculate the steering vectors. For comparison free-field Green's functions were used to calculate the according standard steering vectors. A measurement without rectangular heat exchanger box evaluated with free-field steering vectors was used as reference test case.

A disc equipped with 60 loudspeakers was used as sound source. The measurements were done both stationary and rotating at a rotational speed of $n = 230\,\mathrm{rpm}$. For the present study only one loudspeaker was used. Its radial position $r = 0.43\,\mathrm{m}$ corresponds to a typical outer radius of an axial fan for the given setup. Furthermore, it should be noted that the investigations have been done with white noise. The method has not been tested for tones yet.

Beamforming maps were calculated for both the stationary and the rotating measurements in the frequency range up to $f = 4500$ Hz. Three different cases have been considered: As a reference case, a measurement without heat exchanger box has been evaluated using steering vectors based on the free-field Green's functions. The second and third case is based on the measurement with heat exchanger box. For the second case, the steering vectors have been calculated based on the free-field Green's functions and for the third case based on the BEM-simulated tailored Green's functions.

Based on the beamforming maps and the validation criteria derived from these maps it could be shown that the use of tailored Green's functions improves the beamforming maps for both the stationary and the rotating test cases examined. For three of four validation criteria, the values of the reference measurement without heat exchanger box are reached or even exceeded for most frequencies. Only the levels at the source position deviate from those of the reference measurement.

Possible explanations for the degeneration of the results with heat exchanger box and standard free-field Green's functions were discussed as well as the improvement when using the tailored steering vector. The signal of acoustically shadow microphones can be used by the beamforming algorithm when using matching Green's function which reduces the noise and the main lobe width due the additional useful information. The observed difference between the source levels when using free-field and BEM-simulated Green's functions for the steering vector calculation shows (most probably) the increased sensitive to inaccuracies in the sound propagation when taking reflections, shadowing and diffraction effects into account compared to the known-robust free-field Green's function assumption.

4. Conclusion

In the present work, a method for sound source localization under disturbed propagation conditions has been presented. The method can be used for both stationary and rotating test cases. For stationary cases it operates in the frequency domain and for rotating cases in the time domain, the according method was generalized to incorporated tailored Green's function and their weighting into time domain beamforming. The test case was a fan test bench where a generic source is placed inside a short heat exchanger duct and microphone array measurements were performed outside the duct in a semi-anechoic chamber.

The Green's functions used in this paper were simulated in frequency domain using the Boundary Element Method, considering all reflection, diffraction, and shadowing effects. The numerically determined Green's functions are applied to beamforming on an experimental dataset similar to the numerically simulated.

In the process of validating the resulting maps, several validation criteria were set up for assessment of the effect of the simulated Green's functions versus a free-field monopole assumption. It was shown that for the selected test case the results for both stationary and rotating beamforming can be significantly improved compared to those of free-field beamforming by using numerically calculated Greens functions.

CRediT authorship contribution statement

Marius Lehmann: Conceptualization, Methodology, Software, Formal analysis, Investigation, Data curation, Writing – original draft, Visualization. **Daniel Ernst:** Conceptualization, Methodology, Software, Validation, Writing – original draft, Writing – review & editing. **Marc Schneider:** Conceptualization, Resources, Writing – review & editing, Supervision, Project administration, Funding acquisition. **Carsten Spehr:** Conceptualization, Writing – original draft, Writing – review & editing, Supervision. **Markus Lummer:** Software.

Declaration of competing interest

The authors declare that they have no known competing financial interests or personal relationships that could have appeared to influence the work reported in this paper.

References

[1] B. Barsikow, W. King Iii, E. Pfizenmaier, Wheel/rail noise generated by a high-speed train investigated with a line array of microphones, J. Sound Vib. 118 (1987) 99–122.
[2] R. Merino-Martínez, P. Sijtsma, M. Snellen, T. Ahlefeldt, J. Antoni, C.J. Bahr, D. Blacodon, D. Ernst, A. Finez, S. Funke, et al., A review of acoustic imaging methods using phased microphone arrays, CEAS Aeronaut. J. 10 (2019) 197–230.
[3] P. Sijtsma, S. Oerlemans, H. Holthusen, Location of Rotating Sources by Phased Array Measurements, Report No. NLR-TP-2001-135, National Aerospace Laboratory NLR, 2001.
[4] P. Sijtsma, Using Phased Array Beamforming to Locate Broadband Noise Sources Inside a Turbofan Engine, Report No. NLR-TP-2009-689, National Aerospace Laboratory NLR, 2006.
[5] R. Dougherty, B. Walker, D. Sutliff, Locating and quantifying broadband fan sources using in-duct microphones, in: Proceedings of the 16th AIAA/CEAS Aeroacoustics Conference, Stockholm, Sweden, 2010, http://dx.doi.org/10.2514/6.2010-3736.
[6] G. Herold, E. Sarradj, Microphone array method for the characterization of rotating sound sources in axial fans, Noise Control Eng. J. 63 (6) (2015) 546–551, http://dx.doi.org/10.3397/1/376348.
[7] C. Lowis, P. Joseph, A focused beamformer technique for separating rotor and stator-based broadband sources, in: Proceedings of the 12th AIAA/CEAS Aeroacoustics Conference (27th AIAA Aeroacoustics Conference), Cambridge, Massachusetts, 2006, http://dx.doi.org/10.2514/6.2006-2710.
[8] C.R. Lowis, In-Duct Measurement Techniques for the Characterisation of Broadband Aeroengine Noise (Ph.D. thesis), University of Southampton, 2007.
[9] W. Pannert, C. Maier, Rotating beamforming–motion-compensation in the frequency domain and application of high-resolution beamforming algorithms, J. Sound Vib. 333 (7) (2014) 1899–1912, http://dx.doi.org/10.1016/j.jsv.2013.11.031.
[10] C. Ocker, W. Pannert, Imaging of broadband noise from rotating sources in uniform axial flow, AIAA J. 55 (4) (2017) 1185–1193, http://dx.doi.org/10.2514/1.J055309.
[11] S. Jekosch, E. Sarradj, An extension of the virtual rotating array method using arbitrary microphone configurations for the localization of rotating sound sources, in: Acoustics, Vol. 2, No. 2, Acoustics (2020) 330–342, http://dx.doi.org/10.3390/acoustics2020019.
[12] E. Sarradj, S. Jekosch, G. Herold, An efficient ray tracing approach for beamforming on rotating sources in the presence of flow, in: Proceedings of the 8th Berlin Beamforming Conference, Berlin, Germany, 2020.
[13] S. Guidati, C. Brauer, S. Wagner, The reflection canceller-phased array measurements in a reverberating environment, in: Proceedings of the 8th AIAA/CEAS Aeroacoustics Conference & Exhibit, Breckenridge, Colorado, 2002, http://dx.doi.org/10.2514/6.2002-2462.
[14] J. Fischer, C. Doolan, Beamforming in a reverberant environment using numerical and experimental steering vector formulations, Mech. Syst. Signal Process. 91 (2017) 10–22, http://dx.doi.org/10.1016/j.ymssp.2016.12.025.
[15] P. Sijtsma, H. Holthusen, Corrections for mirror sources in phased array processing techniques, in: Proceedings of the 9th AIAA/CEAS Aeroacoustics Conference and Exhibit, Hilton Head, South Carolina, 2003, http://dx.doi.org/10.2514/6.2003-3196.
[16] J. Fischer, C. Doolan, Improving acoustic beamforming maps in a reverberant environment by modifying the cross-correlation matrix, J. Sound Vib. 411 (2017) 129–147, http://dx.doi.org/10.1016/j.jsv.2017.09.006.
[17] S. Bousabaa, Acoustic Green's Function Estimation using Numerical Simulations and Application to Extern Aeroacoustic Beamforming (Ph.D. thesis), Sorbonne Université, 2018.
[18] M. Kaltenbacher, B. Kaltenbacher, S. Gombots, Inverse scheme for acoustic source localization using microphone measurements and finite element simulations, Acta Acust. United Acust. 104 (4) (2018) 647–656, http://dx.doi.org/10.3813/AAA.919204.
[19] S. Gombots, M. Kaltenbacher, B. Kaltenbacher, Inverse scheme for acoustic source localization in 3D, in: Proceedings of Euronoise, Heraklion, Crete - Greece, 2018.
[20] S. Gombots, M. Kaltenbacher, B. Kaltenbacher, Combined experimental-simulation based acoustic source localization, in: Proceedings of DAGA, Aachen, Germany, 2016.
[21] P. Sijtsma, Experimental Techniques for Identification and Characterisation of Noise Sources, Report No. NLR-TP-2004-165, National Aerospace Laboratory NLR, 2004.
[22] P. Welch, The use of fast Fourier transform for the estimation of power spectra: A method based on time averaging over short, modified periodograms, IEEE Trans. Audio Electroacoust. 15 (2) (1967) 70–73, http://dx.doi.org/10.1109/TAU.1967.1161901.
[23] E. Sarradj, Three-dimensional acoustic source mapping with different beamforming steering vector formulations, Adv. Acoust. Vib. 2012 (2012) http://dx.doi.org/10.1155/2012/292695.
[24] J.W.S.B. Rayleigh, The Theory of Sound, Vol. 2, Macmillan, 1896.
[25] M. Lummer, Installation: numerical investigation, CEAS Aeronaut. J. 10 (2019) 159–178, http://dx.doi.org/10.1007/s13272-019-00382-5.
[26] M. Lummer, R.A. Akkermans, C. Richter, C. Pröber, J. Delfs, Validation of a model for open rotor noise predictions and calculation of shielding effects using a fast BEM, in: Proceedings of the 19th AIAA/CEAS Aeroacoustics Conference, Berlin, Germany, 2013, http://dx.doi.org/10.2514/6.2013-2096.
[27] R. Ruck, Entwicklung einer schallausbreitungssimulation unter verwendung der fast multipol boundary element method (FM-BEM) (development of a sound propagation simulation using the fast multipol boundary element method), 2019, Technische Hochschule Nürnberg.